# Impact of Measurement Points Distribution on the Parameters of UWB Implant Channel Model

Sofia Perez-Simbor[1], Katjana Krhac[2], Concepcion Garcia-Pardo[1], Kamran Sayrafian[3], Dina Simunic[2], Narcis Cardona[1]

*Abstract*—Sophisticated medical implants that allow vital information delivery to/from the human body are opening the door to novel approaches in diagnosis and/or therapy of various health related issues. Ultra-Wide Band (UWB) technology is gaining the attention of researchers as a possible candidate for implant communication due to its high data rate and low power consumption capabilities. Characterization of a propagation channel often involves a measurement campaign (either virtual or physical) and selecting a set of candidate test points (i.e. sample measurement points) through which numerical values of the desired signal at the receiver are collected. Statistical analysis of those data will lead to a channel model representing the communication link. Focusing on UWB implant channel characterization, this paper aims to highlight the potential impact of the measurement points location distribution on the extracted parameters of the channel model. This is achieved through emulating a custom-design multi-layer liquid phantom measurement system and performing a sequence of matching simulations with different sample point distributions. The results are meant to serve as a guideline for future UWB implant measurement campaigns.

*Keywords*— Ultra-Wide Band (UWB); Body Area Network (WBAN); phantom measurements; statistical channel models.

## I. INTRODUCTION

A Wireless Body Area Network (WBAN) is a relatively new technology that has been developed to connect wearable or implantable sensors/actuators located inside or on the surface of the human body. IEEE802.15.6 is the first international standard that outlines the frequency bands that can be used for different use-cases in a WBAN [1]. The most common frequency bands that are used for WBAN applications are 402–405 MHz (i.e. Medical Implant Communication Service (MICS)), 2.4–2.4835 GHz (Industrial, Scientific and Medical radio band (ISM)) and 3.1 to 10.6 GHz (unlicensed Ultra-Wide Band (UWB)).

At present, and as described in the IEEE802.15.6 standard, for implant or equivalently in-body communication (i.e. communication to a node inside the human body) only MICS frequency band has been considered. Maximum data rate that can be achieved using this band is 455 kbps [1]. However, some recent applications such as video capsule endoscopy could require much higher data rates in order to be able to deliver better quality images from the human Gastrointestinal (GI) tract. For this reason, researchers are also considering the UWB technology for in-body communication. An UWB signal is known to suffer from high propagation loss inside the human body. However, high data rate capability along with low transceiver complexity as well as the possibility for miniature size antennas would still make this technology an attractive candidate for in-body applications [2].

There are several recent studies in the literature on UWB channel characterization and statistical modeling for implant communication [3,4,5]. The frequency dependence of the channel has been shown and studied using simulation in [6]. Since *in-vivo* experimentation is either difficult or in case of human subject nearly impossible, commonly used approaches to study implant UWB channels is through either computational or liquid phantom measurements. Liquid phantoms are aqueous solutions that precisely mimic the electromagnetic properties of the human tissues. Therefore, they enable researchers to conduct physical measurements to study an implant channel in a laboratory environment. A comprehensive measurement campaign using a custom built multi-layer phantom for UWB frequency band has been done in [3]. Whether through simulation or experimental measurement, the process to study UWB implant channels include defining a set of measurement points (i.e. grid) that will result in sample numerical measurements from the channel. The measurement results will be processed further to acquire knowledge about the channel characteristics. Typically, these measurement points are based on a regular spacing of several locations (e.g. a rectangular grid) where either the transmitter or receiver are positioned. Although, this is a common methodology in most wireless channel characterization efforts, for the case of UWB implant channel (and due to the short distances under which the communication link is operational), special care is needed to consider a proper set of sample measurement point locations.

In this paper, using the results in [3] and a sequence of matching simulations, the impact of sample measurement points on the extracted channel model is

---

[1]Universitat Politècnica de València (UPV), Spain
[2]University of Zagreb, Croatia
[3] National Institute of Standards & Technology, USA

studied. This study is meant to lay the groundwork for future measurements and design of an optimal set of sample point locations to obtain UWB implant channel models.

This paper is organized as follows. Section II describes the hardware measurement set up and the equivalent virtual model for the multi-layer phantom. Section III provides a brief overview of the methodology and the statistical analysis used to process the results. The potential impact of sample measurement points distribution on the extracted parameters of a pathloss model is discussed in section IV. Finally, Conclusions and future work are provided in section V.

## II. MEASUREMENT & COMPUTATIONAL SETUP

### A. Physical Measurement System

Figure 1 shows the main elements of the measurement setup developed at the Universitat Politècnica de València (UPV). The setup consists of an anechoic chamber, Vector Network Analyzer (VNA), a 3D spatial positioner, a phantom container, a magnetic tracker and finally a laptop. Most of the elements are connected to the laptop and controlled by a specialized software. The anechoic chamber is used to minimize potential impact of reflections due to the surrounding environment. The chamber has an internal volume of $1 \times 1 \times 1$ m$^3$ built in a wooden structure with 22 mm width.
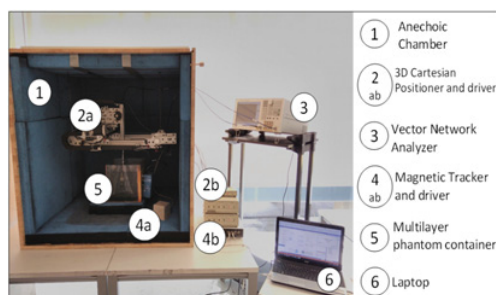


Fig. 1. Experimental Setup

A 3D Cartesian positioner is placed inside the anechoic chamber (Fig. 1 element 2a) to allow calculation of the relative distances between receiver and transmitter antennas. This positioner has a 1 mm precision along the X, Y, and Z axes and $30 \times 30 \times 10$ cm$^3$ movement range. The in-body antenna is attached to the positioner in this measurement setup. In addition to the 3D positioning system, the spatial position of each antenna is calculated by a 3D magnetic tracker using sensors that are attached to the center of each antenna (Fig. 1, element 4b).

The multi-layer phantom container (shown in Fig. 1 element 5) is made of polyethylene terephthalate (PET) material with a width of 1.5 mm and has an overall internal volume of $25 \times 25 \times 25$ cm$^3$. The container consists of two layers (i.e. segments) of muscle and fat liquid phantoms with dimensions of $23 \times 25 \times 25$ and $2 \times 25 \times 25$ cm$^3$ respectively. A divider sheet also made of PET (with 1.5 mm thickness) separates the liquid phantom layers. The walls of the container are made as thin as possible in order to have minimum impact on the signal propagation inside the multi-layer phantom. The liquid phantoms used in this experiment accurately mimic the electrical properties of the human muscle and fat tissues for the entire UWB frequency band [8]. Since the phantoms properties vary with temperature, the experiments were carried at a controlled temperature of 24ºC. The UWB antennas used in the experiment are patch antennas with a quasi-omnidirectional radiation pattern [8]. Their dimensions are 2.3 cm × 2 cm (in-body) and 5 cm × 4.4 cm (on-body) respectively. Further details of the measurement system can be found in [3].

### B. Computational Measurement System

Extensive computational time and high memory requirements often create an obstacle in performing sophisticated electromagnetics simulations to study a UWB wireless channel. However, such simulations are helpful to gain an idea about the general behavior of a wireless link or identify appropriate scenarios to perform physical measurements. Using a dedicated computer with 64 cores and 3 TB of memory, the core elements of the physical measurement system described in the previous subsection (i.e. the container along with the liquid phantom layers) was emulated using ANSYS HFSS[4] (see Fig. 2) at the Information Technology Laboratory of the National Institute of Standards and Technology (NIST). The simulated container has identical dimensions, thickness and material properties as the one shown in Fig. 1 element 5. The simulated container also includes the divider sheet that separates the fat and muscle phantoms in the experiment. Each segment of the container is then filled with muscle and fat tissues. The corresponding frequency-dependent material properties of these tissues are programmed to be identical to the liquid phantoms used in the experiment.
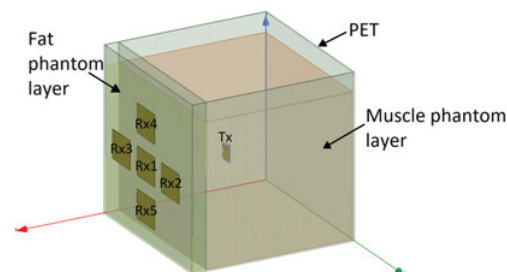


Fig. 2. Simulated phantom container

In addition, models of the UWB receiver and transmitter antennas that were used in the experiment

---

[4] HFSS is a product of ANSYS, Inc. HFSS has been used in this research to foster research and understanding. Such identification does not imply recommendation or endorsement by the National Institute of Standards and Technology, nor does it imply that this product is necessarily the best available for the purpose.

have also been developed in HFSS. Fig 3 shows the measured and simulated reflection coefficient of both antennas (i.e. S11) inside the muscle phantom for the frequency range 3.1-4.1 GHz.



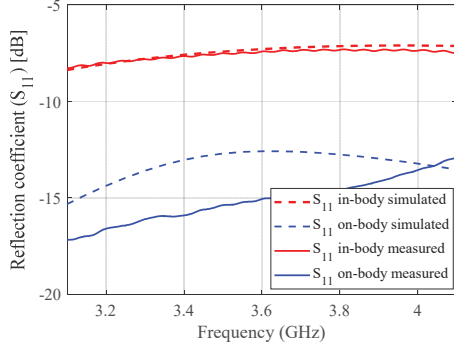Fig. 3. Measured & Simulated S11 of the transmitting and the receiving antennas

To evaluate the simulation system, the magnitude of the forward transmission coefficient (i.e. $S_{21}$) obtained through measurement and simulation were compared for a given receiver and several transmitter positions that are located at 5.5, 6.5, 7.5 and 8.5 centimeters away from the receiver. The receiver (i.e. on-body) antenna is located on the external side of the fat phantom layer while the transmitter (i.e. in-body) antenna is placed at the above distances facing the receiver antenna on a horizontal line in the center of the container. As observed in Fig. 4, there is a relatively good agreement among the measured (solid lines) and simulated (dashed lines) $S_{21}$ values versus distance.
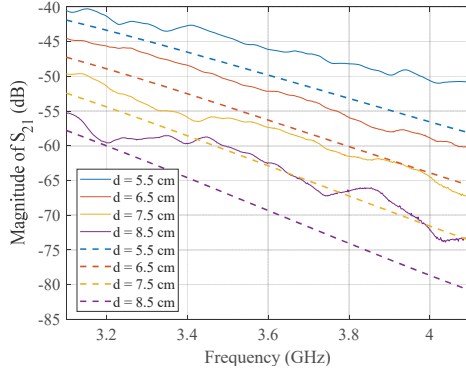


Fig. 4. Comparison of $S_{21}$ vs. frequency at various distances between the transmitter and Receiver

In the measurement process, there is slight misalignment of the antennas due to different elevations (i.e. height) of the receiver and transmitter positions; however, in the simulations, both receiver and transmitter are on the horizontal plane and completely facing each other (i.e. no misalignment). This misalignment causes the relative antenna pattern orientations between the receiver and transmitter to be

different. This in turn will impact the resulting measured S21s values. Also, the slight difference in elevation between the receiver-transmitter means that the actual distance between the pair is slightly higher than the specified X-axis deviations of 5.5 through 8.5 centimeters. The combination of these two issues has therefore resulted in slight differences among the observed numerical values of the simulation versus measurements in Fig. 4.

## III. METHODOLOGY & STATISTICAL ANALYSIS

The robotic positioner along with the magnetic tracker can be used to place the in-body antenna at various 3D locations inside the muscle layer of the container. These locations collectively define a grid of sample points that are used to conduct measurement for quantities such as $S_{21}$. The measurement results are further analyzed to obtain a statistical pathloss model. Typically, the measurement grid is set up in a uniform rectangular (or cubical in 3D) lattice with a certain resolution in the X-Y plane (or X-Y-Z in 3D). An example of such an arrangement for sample point measurements in the multi-layer container is shown in the Fig. 5.
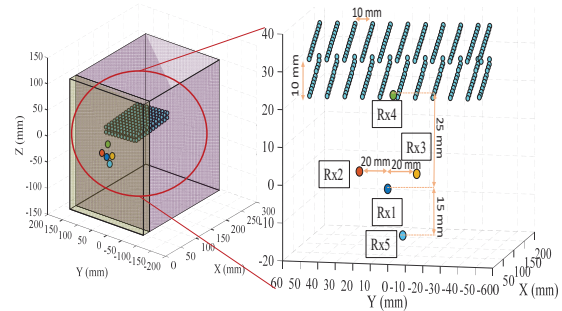


Fig. 5. Measurement Grid Setup

As observed, there are 2 rectangular lattices at different elevations where each point on the lattice indicates a sample measurement location for the in-body antenna (light blue circles). The spatial resolution between sample points in the X, Y and Z plane is 1 cm. The receiver (i.e. on-body antenna) locations are shown using different color circles located on the Y-Z plane and numbered 1 through 5. Using the above measurement grid points and a distance and frequency-dependent logarithmic pathloss model (1), a statistical analysis was performed on the set of the sample $S_{21}$ measurement points.

$$PL^{dB}(f) = PL_0^{dB}(f) + 10n(f)log_{10}\left(\frac{d}{d_o}\right) + N(\mu, \sigma) \quad (1)$$

In (1), n(f) is the frequency dependent pathloss exponent and $N(\mu,\sigma)$ captures the random variation of pathloss around its mean due to antenna gain pattern, reflections, refractions or multipath.

For each sample antenna position on the grid, the pathloss between the transmitter and the receiver is

calculated for the frequency range 3.1-4.1 GHz as (2).

$$PL^{dB}(f) = -10log_{10}|S_{21}(f)^2| \quad (2)$$

Table 1 shows the average pathloss exponent (denoted by $\overline{n(f)}$) for the frequency range 3.1 to 4.1 GHz for each receiver location.

TABLE I. Average Pathloss Exponent

| | $\overline{n(f)}$ |
|---|---|
| RX1 | 9.49 |
| RX2 | 9.90 |
| RX3 | 10.46 |
| RX4 | 9.88 |
| RX5 | 11.50 |

Although, some variation of the pathloss exponent with respect to frequency can be expected, its dependency on the receiver position might not be expected at the first glance. However, a detailed look at the geometry of the measurement grid indicates that this dependency is the direct result of the relative distances of the sample points on the grid with respect to each receiver's position. In fact, it can be shown that not only the set of transmitter-receiver distances for each receiver position could be different, but also the distribution of the distances (which generates the scatter plot where the logarithmic statistical model (1) is derived from) is also different. To elaborate on this issue, Fig. 6, highlights the histogram of relative distances of all the sample measurement points for each of the five receiver's locations.
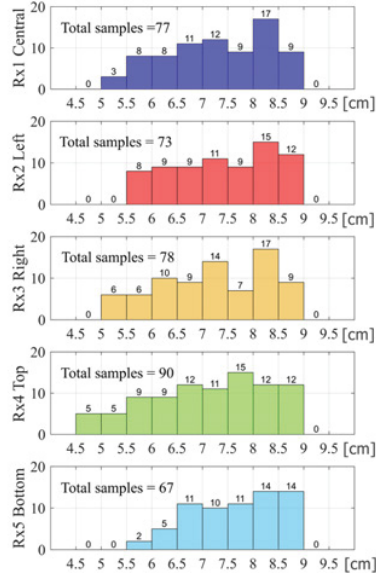


Fig. 6. Distribution of the sample measurement point per receiver location

The non-identical distribution of the distances resulting from the transmitter positions on the grid directly impacts the extracted parameters of the statistical pathloss model i.e. n(f). In addition, the non-uniform nature of each distribution could also impact the extracted parameters for each individual receiver. This issue was further studied using the multi-layer phantom simulation platform and the results are summarized in the next section.

IV. IMPACT OF GRID POINT DISTRIBUTON

To study the impact of the measurement grid and the resulting sample point distribution, two different grids were set up in the virtual model of the multi-layer phantom as shown in Fig 7.
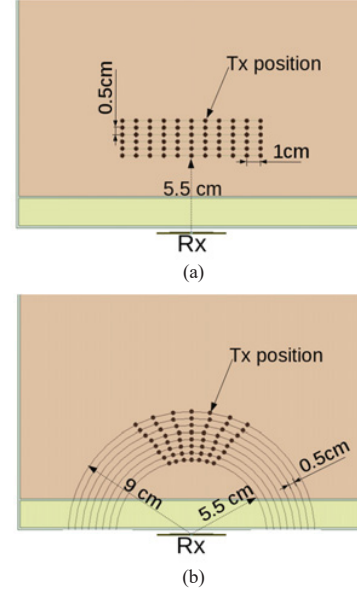


Fig. 7. (a) Sample Rectangular Measurement Grid (b) A Circular Measurement Grid

The rectangular grid is set up through a uniform rectangular lattice with 0.5 cm spacing on the x-axis and 1 cm spacing on the y-axis. To increase the number of sample points, two or more levels of this rectangular grid (i.e. with different elevations) can be considered for simulation purposes. Here, to minimize the impact of antenna orientation on the results, only one level of grid points (at the same elevation as the receiver) was considered. The actual distances between grid points and the receiver location (i.e. the distance between the center of the in-body and on-body antenna) will result in the histogram shown in Fig. 9(a).

On the other hand, the circular grid is set up through intersection of circles (co-centered at the receiver location) with different radii as observed in Fig. 7(b). The spacing between circles as well as angular spacing among different radii can be variable and chosen according to the requirement of the statistical model in consideration. In this study, the spacing between circles was chosen to be 0.5 cm; and, to minimize the impact of antenna orientation on the extracted parameters, small angular

spread was considered. The circular grid shown in Fig. 7(b) will result in the transmitter-receiver distance histogram in Fig 9(b). In general, the final set of grid points do not necessarily have to lie on any circles; instead they can be located in between circles spacing (e.g. Fig. 8). This pattern will also lead to a uniform distance histogram as shown in Fig. 9(b).
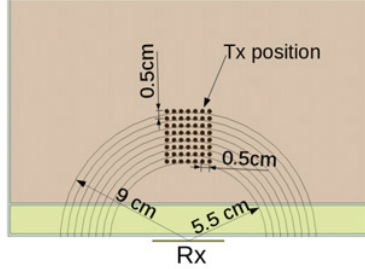


Fig. 8. Another example of Circular Measurement Grid

Simulations with the virtual model of the multi-layer phantom were performed using both types of grids shown in Fig 7 to obtain the $S_{21}(f)$ values for frequency range of 3.1 to 4.1 GHz. It should be noted that at each grid point the in-body antenna was facing parallel to the receiver and no antenna rotation was considered at any points. Through statistical analysis of these data, and again assuming the pathloss model in (1), the average pathloss exponent $(\overline{n(f)})$ was obtained and presented in Table 2.
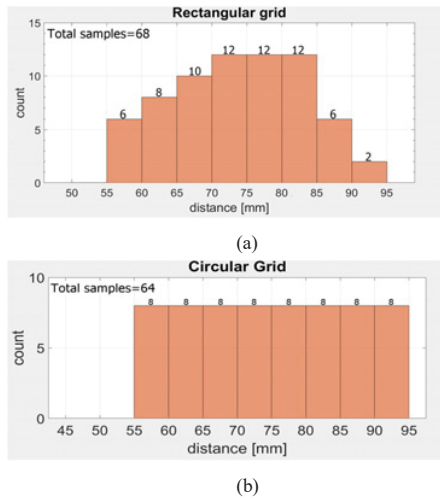


(a)



(b)

Fig. 9. Histogram of the TX-RX distances in the (a) Rectangular Grid (b) A Circular Grid

TABLE II. AVERAGE PATHLOSS EXPONENT FOR DIFFERENT GRIDS

| | $\overline{n(f)}$ |
|---|---|
| Rectangular Grid | 9.68 |
| Circular Grid | 10.60 |

The results show the potential impact of the measurement points distribution on the extracted pathloss exponent. The circular grid leads to a more uniform distribution of sample point distances; and therefore, all samples are fairly and equally represented during the statistical analysis process. This in turn could lead to more accurate channel model parameters. Mathematical nature of the statistical model could also provide additional input on the grid points selection; for example, logarithmic based models might benefit from logarithmic scale for circles spacing in the circular measurement layout. The characteristics of the specific implant application in consideration can provide the overall guidelines on the arrangement and selection of optimal grid points before the measurement process.

## V. CONCLUSIONS

Through a joint simulation and experimentation study, this paper highlights the potential impact of sample measurement points location and distribution on the extracted parameters of a statistical channel model such as a frequency dependent pathloss exponent. It is shown that for studying a UWB implant channel a judicious selection of measurement points could lead to a sample set that better represents the transmitter-receiver distances as well as relative antenna pattern orientation. This process will result in a more accurate statistical model for the communication channel. To the best of our knowledge, there are no similar studies in the literature for UWB implant channels.

Although only the impact on pathloss exponent was considered in this study, we conjecture similar impact exist on other parameters of the statistical model that are obtained through the fitting process. For example, better representation of the sample measurement points could lead to a more accurate $N(\mu, \sigma)$ which captures random variations of the pathloss around the mean value in (1). The short communication distances and limited number of measurement points are among the reasons that differentiates implant communication with any other wireless channels. In general, the specifics of the intended use-case should drive the selection of sample measurement points for such channel modeling efforts. The authors plan to do more physical measurements using similar UWB multi-layer phantom and continue this research following an optimally designed measurement grid.

## REFERENCES

[1] IEEE Standards Association, *IEEE Standard for Local and metropolitan area networks - Part 15.6: Wireless Body Area Networks*, February. 2012.

[2] A. Ghildiyal, K. Amara, R. D. Molin, B. Godara, A. Amara, and R. K. Shevgaonkar, "UWB for in-body medical implants: A viable option," in *2010 IEEE International Conference on Ultra-Wideband*, 2010, pp. 1–4.

[3] S. Perez-Simbor, M. Barbi, C. Garcia-Pardo, S. Castelló-Palacios, N. Cardona, "Initial UWB In-Body Channel Characterization Using a Novel Multilayer Phantom Measurement Setup", *2018 IEEE Wireless Communications and Networking Conference Workshops (WCNCW)*, Barcelona, 2018, pp 384-389

[4] C. Garcia-pardo, C. Andreu, A. Fornes-leal, S. Perez-simbor, M. Barbi, A. Vallés-Lluch and N.Cardona, "Ultrawideband Technology for Medical In-Body Sensor Networks: An Overview of the Human Body as a Propagation Medium, Phantoms, and Approaches for Propagation Analysis ," in *IEEE Antennas and Propagation Magazine*, vol 60, no. 3, pp. 19-33, June 2018.

[5] J. Wang and Q. Wang, "Channel modeling and BER performance of an implant UWB body area link," *2009 2nd International Symposium on Applied Sciences in Biomedical and Communication Technologies,* Bratislava, 2009, pp. 1-4

[6] M. Kanaan and M. Suveren, "A novel frequency-dependent path loss model for ultra-wide band implant body area networks," Measurement, vol. 68, pp. 117-127, 2015

[7] N. Cardona, S. Castelló Palacios, A. Fornés Leal, C. García Pardo, and A. Vallés Lluch, "Synthetic Model of Biological Tissues for Evaluating the Wireless Transmission of Electromagnetic Waves," Patent WO/2017/109252, 2017

[8] C. Andreu, C. Garcia-Pardo, A. Fornes-Leal, M. Cabedo-Fabrés, and N. Cardona, "UWB In-Body Channel Performance by Using a Direct Antenna Designing Procedure," *2017 11th European Conference on Antennas and Propagation (EUCAP)*, Paris, 2017, p. 278-282.